


Laser ablation of a Cu–Al–Ni combinatorial thin film library: analysis of crater morphology and geometry

Simina Aurelia Rebegea¹ · Keith Thomas² · Vipin Chawla² · Johann Michler² · Ming Chu Kong¹ 

Received: 18 November 2016 / Accepted: 22 November 2016 / Published online: 5 December 2016
© The Author(s) 2016. This article is published with open access at Springerlink.com

Abstract The conventional approach to studying laser–workpiece interaction in the ablation regime is to vary beam parameters used on a specimen of uniform chemical composition. The current work instead utilises a pulsed laser beam of constant parameters to ablate a ternary alloy thin film where the chemical composition of the sample varies continuously; this will enhance the understanding of pulsed laser ablation by means of a combinatorial approach. The analysis of the studied workpiece (a Cu–Al–Ni thin film deposited by magnetron sputtering) revealed the presence of both compositional and morphological gradients. Variation in the surface morphology was correlated with aluminium content. Single-pulse laser ablation (Nd:YAG, 1064 nm, 30 ns, 4.54 J/cm²) of the surface resulted in different crater features, geometry and volume. Two characteristic regions separated by a transition zone were identified based on the craters’ geometrical and morphological characteristics. The ablated volume increases with the atomic percentage of aluminium up to a threshold value of roughly 30 at.% after which the ablation volume slowly declines. This phenomenon may be attributed to plasma absorption and heat dissipation in the thin film.

1 Introduction

Laser-based technologies are gaining ground in the manufacturing industry as non-conventional machining processes as they allow precise machining of micron and submicron features in otherwise difficult-to-machine materials (e.g. ceramics, semiconductors). Several advantages of using lasers for material processing are: (1) no contact between the tool and the workpiece, resulting in no tool wear and reduced chance of damage to the processed material caused by handling; (2) no chemicals are used, which makes it environmental friendly; (3) selective material removal can be achieved by choosing a particular combination of wavelength and energy, causing limited damage to the under-layers. In machining processes, lasers can be used for microdrilling, fine cutting, milling and reshaping.

Despite the advantages of laser micromachining over other conventional or non-conventional methods [1, 2], the complex nature of the laser beam–material interaction makes the exact outcome of laser ablation difficult to predict [3, 4]. For example, changing the beam parameters (e.g. wavelength, temporal pulse width) affects how the energy transfer between the laser and the surface takes place, as does the variation in material characteristics (e.g. absorption coefficient and thermal conductivity).

Given the many variables that can change the material response in laser ablation, numerous studies are dedicated to gaining a better understanding of this phenomenon. Both empirical and theoretical studies have already been performed, each taking into consideration various physical parameters of the laser beam and material properties. Some of the previous experimental studies explore the dynamics involved, investigated by either time-resolved techniques [5], imaging of the process with fast ICCD cameras [6],

✉ Ming Chu Kong
C.Kong@bham.ac.uk

¹ School of Engineering, Room S10A Mechanical and Civil Engineering Building (Y3), University of Birmingham, Edgbaston, Birmingham B15 2TT, UK

² Laboratory for Mechanics of Materials and Nanostructures, EMPA, Swiss Federal Laboratories for Materials Testing and Research, Feuerwerkerstrasse 39, 3602 Thun, Switzerland

time-of-flight measurements [7] or analysis of the plume expansion [8].

Although these studies cover a wide range of materials including pure metals [9], alloys [10], semiconductors [11] and optical transparent materials [12], their common ground is the approach used to study the laser–material interaction. Samples of uniform chemical composition with well-known optical and thermal properties are ablated while various beam parameters (e.g. fluence, pulse duration and wavelength) are varied. This study instead investigates the role which initial material morphology and a chemical composition gradient across the workpiece play in pulsed laser ablation.

The aim of the current work is to offer a novel approach to the investigation of material response (in terms of crater geometry, volume removal and sub-surface morphology) in pulsed laser ablation by using a material library (sample with continuous variation in the chemical composition) and irradiating it with a beam of constant parameters. This combinatorial approach provides improved understanding of the pulsed laser interaction with a range of Cu–Al–Ni alloys, potentially enabling novel scientific and engineering applications.

2 Materials and methods

We report one of the first studies which use the combinatorial approach to investigate laser ablation of a ternary copper–aluminium–nickel alloy thin film using a single laser pulse of constant parameters (fluence, wavelength and temporal width). The choice of alloy for the experiments carried out in this work is based on the individual material properties relevant to the ablation process, as well as on the potential shape memory behaviour these three metals combined may exhibit.

Dictated by the variations which naturally exist in material libraries, the first part of this paper is aimed at the characterisation of the as-deposited thin film. Measurements of reflectivity, elemental distribution and thin film thickness prior to irradiation are relevant to nanosecond pulsed laser ablation (“thermal regime”), and they are used for a qualitative analysis of the single-pulse ablated craters. Subsequently, micrographs obtained by electron microscopy are used to illustrate the variations in both the thin film sample (prior to ablation) and its crater morphology (after ablation). The variations in the crater morphology and geometry are discussed with respect to the optical characteristics of the parent material, its elemental distribution and the physical properties of Cu, Al and Ni. Profiles and ablated volume of the ablation sites are obtained by 3D optical microscopy and used to quantify the ablation result.

2.1 Deposition of thin film with compositional gradients

The ternary compositional gradient film used in this study was deposited on a 4-inch diameter silicon (100) wafer, in a magnetron sputtering facility (Mantis Deposition Ltd, UK, Model: QPrep). The targets used were aluminium, copper and nickel (99.95, 99.99 and 99.95% purity, respectively) and were sputtered simultaneously at different discharge powers to achieve the desired composition (RF—173 W, DC—67 W, DC—28 W, respectively). A turbo-molecular pump backed by a dry rotary pump ensured a base pressure of 2×10^{-4} Pa. The gradient was obtained by decreasing the target-to-substrate distance (8 cm) and without substrate rotation, in argon atmosphere (Ar = 45 sccm, 0.3 Pa) and at room temperature (Fig. 1a).

2.2 Thin film characterisation

Mapping of the chemical composition was done by energy-dispersive X-ray (EDX) spectroscopy, equipped on a Philips XL30 scanning electron microscope. Certified microanalysis standards (Oxford Instruments Link ISIS EDX microanalysis system) were used for the quantification of the three elements with an acquisition time of 60 s.

Surface characterisation of the as-deposited thin film was performed by high-resolution electron microscopy

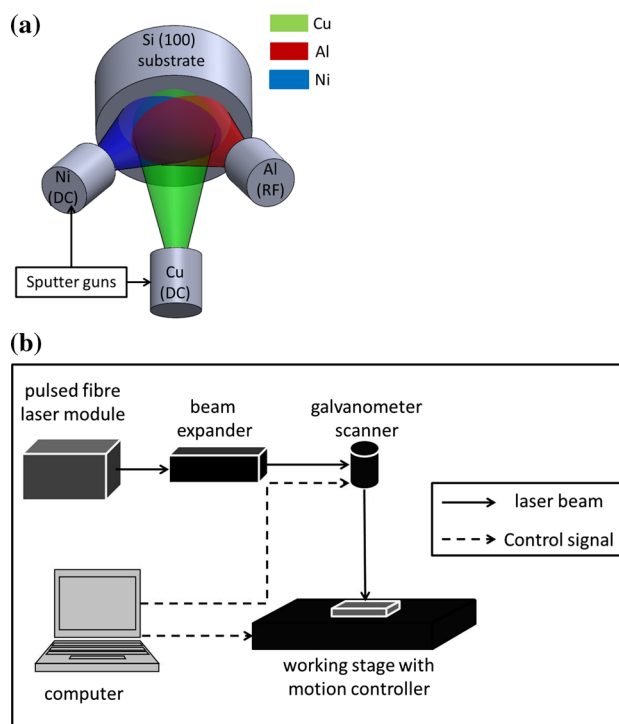


Fig. 1 Schematic representation of **a** the sputtering set-up and **b** the experimental laser set-up

(SEM Hitachi S480, acceleration voltage 1.5 kV) and atomic force microscopy (AFM NT-MDT Solver Pro-M operating in tapping mode, using a nominal tip radius with 15 nm radius of curvature). Topographic parameters (i.e. root mean square roughness and height–height correlation length) were obtained from the $10 \times 10 \mu\text{m}^2$ AFM scans using Gwyddion software. The size of surface features was determined from the micrographs using *ImageJ* software. The measurement of the total reflectivity R (%) was performed at 15 areas on the sample (shown in Fig. 2), with a Perkin Elmer UV/VIS/NIR Lambda 900 spectrophotometer, using a 5×10 mm rectangular spot.

2.3 Single-pulse laser ablation of the material library

The experiments were carried out using a SPI G4 20 W HS Series L Type air-cooled nanosecond pulsed fibre laser module, operating at 1064 nm (Fig. 1b), with a focused spot size diameter of $49.8 \mu\text{m}$. The experiments were performed in air at atmospheric pressure.

The target surface was treated as consisting of 72 square areas, each with 5 mm side length, in an 8×9 matrix (Fig. 2). Within a given area a_{ij} , the chemical composition varies by less than 1 at.%. Therefore, the chemical composition within a matrix area was considered constant. The brighter coloured areas designated in Fig. 2 were chosen for further investigation in order to cover the full compositional spread while maintaining a manageable number of experiments. Each area has a line of individual craters ablated using a constant laser fluence of 4.54 J/cm^2 and pulse duration of 30 ns (optimised to prevent the crater

from penetrating the substrate), separated by adjustment of the machine feed speed to avoid crater overlapping.

2.4 Crater analysis

Crater geometry was measured with *Alicona InfiniteFocus*, an optical 3D microcoordinate system based on focus variation method. A magnification of $20\times$ was used, with a corresponding resolution of 50 nm vertically and $2.93 \mu\text{m}$ laterally. The ablated volume per crater in any area of constant chemical composition was calculated by averaging the values measured in 10–12 different craters. The analysed craters were chosen away from the line ends to avoid the distortions in laser footprint which can occur at the beginning and end of each line on account of acceleration/deceleration in the feed speed. The **resultant ablated volume** is the difference between the crater volume beneath the surface and the volume of the rim of re-solidified material, which rises above the target surface (Fig. 3).

Cross sections of the ablated craters were then prepared via focused ion beam (FIB) using a dual-beam SEM-FIB Tescan Vela instrument in a two-step approach. First, a rough cutting step with high Ga ion beam (30 kV beam and 3 nA probe current) was used to mill a rectangular trench, followed by a fine polishing step (30 kV and 1 nA) in the area of interest.

3 Results and discussion

The 30-ns IR laser irradiation of a metal thin film places the ablation process in the thermal regime, which consists of three main steps. (1) Laser radiation is absorbed by the workpiece in an area under the surface equal to the skin depth (several nm in the case of metals irradiated with IR), and the amount of energy delivered to the sample is directly related to its reflectance at the laser wavelength (1064 nm). (2) The energy is then distributed to the rest of the material by heat transfer. The maximum temperature

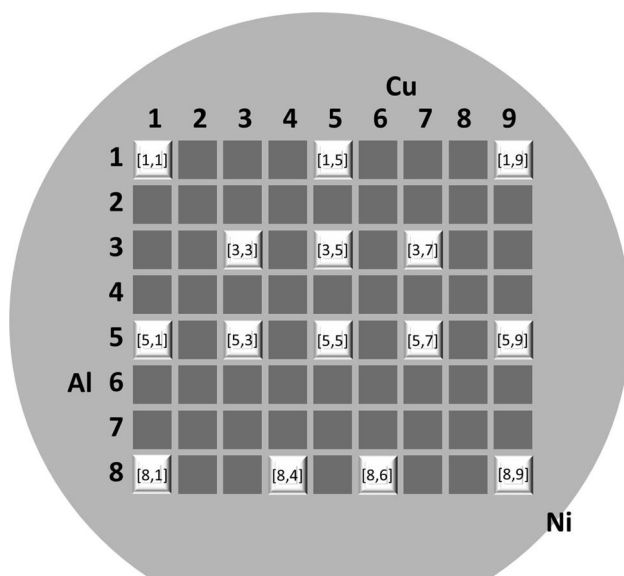


Fig. 2 Laser processing and analysis. The position of the sputtering targets with respect to the substrate is shown

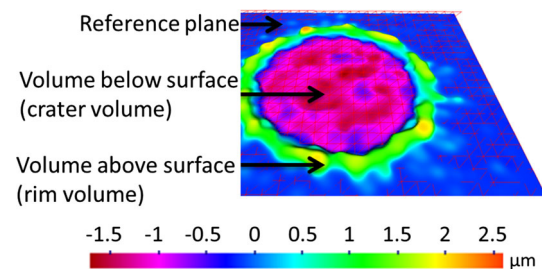


Fig. 3 Schematic representation of volume measurement. The reference plane parallel to the surface splits the crater into two parts: removed material beneath the surface (*crater volume*) and re-solidified material that rises above the target surface (*rim volume*)

and depth are dictated by the thermal properties (e.g. thermal diffusivity, fusion and boiling points, melting and evaporation enthalpies) of the thin film, as well as the surface morphology and topography. Particularly in the case of thin films, heat transfer is influenced by the thickness of the thin film, substrate type and the nature of the interface between the two. (3) Significant ablation occurs when the surface reaches the vaporisation temperature, or even sooner (around the melting point), depending on the pressure at the target surface. Depending on the laser pulse duration and thermal properties of the thin film, heat transfer to the substrate may become important and lead to the ablation of both film and substrate.

In order to study the laser–material interaction on a compositional spread, it is essential to understand the workpiece properties prior to laser irradiation. However, the published information about the material properties (e.g. reflectivity), particularly on such a broad range of chemical compositions, is very limited, and the synthesis technique itself can lead to different material properties and surface morphology. Hence, the first part of the paper focuses on the as-deposited sample characterisation.

3.1 Chemical composition and thin film thickness

The compositional range covered by the sample is shown superimposed on a ternary diagram for the Cu–Al–Ni system in Fig. 4. Films deposited via sputtering often form metastable and non-equilibrium phases which are not represented in a phase diagram generated by slow cooling, so it is quite possible that the phases present within the sputtered film differ from those shown here. The

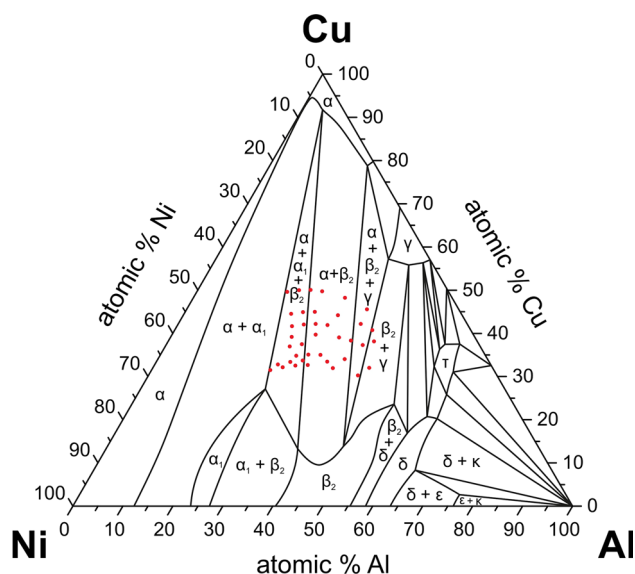


Fig. 4 Ternary Cu–Al–Ni diagram adapted from [21] showing the region covered by this compositional gradient sample

equilibrium phases present at these chemical compositions represent a good starting point for analysis and are given in Table 1.

The sample thickness varied between 1 and 1.35 μm and was used as a reference when analysing crater depth. Previous experiments on laser ablation of metallic thin films have demonstrated that the ablation threshold increases linearly with the film thickness up to the thermal diffusion length, after which it remains constant [13]. A simple calculation of the thermal diffusion length for each of the elemental film components is useful for understanding heat transfer in these experiments. Using a film thickness of 1 μm and a pulse duration $\tau = 30$ ns, the thermal diffusion length ($\delta_{\text{th}} = \sqrt{2\tau\alpha}$, thermal diffusivity $\alpha = k/\rho c$, with k the thermal conductivity, ρ the density and c the specific heat) is $\delta_{\text{th-Cu}} = 2.60$ μm , $\delta_{\text{th-Al}} = 2.25$ μm and $\delta_{\text{th-Ni}} = 1.16$ μm for copper, aluminium and nickel, respectively (thermal diffusivity at room temperature taken from [14]). As the film thickness is less than the thermal diffusion length and the beam diameter in focus is around 50 μm , heat conduction is effectively unidimensional and the thermal behaviour of the system is affected by the properties of silicon, with the substrate acting as a heat sink in these experiments.

3.2 Film reflectivity

The initial process defining the laser–workpiece interaction is absorption of radiation. The total reflectivity at 1064 nm wavelength (Fig. 5) across the sample is a measure of the amount of energy absorbed by the material and has a significant influence on the amount of material removed. The overall reflectivity decreases with aluminium content (for concentration see Fig. 4); the area richest in Al has the lowest reflectivity ($R \sim 30\%$) and will thus absorb a higher amount of the incoming laser radiation compared to the area with least Al ($R \sim 70\%$). These values are found to be generally lower than the overall values for reflectivity of the three metals at 1064 nm (Cu $\sim 90\%$, Al $\sim 80\%$ and Ni $\sim 70\%$ of the incident radiation [15]). The optical properties of a material are not determined solely by chemical composition; therefore, surface microstructure

Table 1 Expected equilibrium phases present in chemical composition range covered by sample

Symbol	Phase	Structure
α	Ni–Cu	FCC solid solution
α_1	$\text{Ni}_3\text{Al–Ni}_2\text{CuAl}$	FCC superlattice
β_2	NiAl	BCC superlattice
γ	Cu_9Al_4	Complex cubic

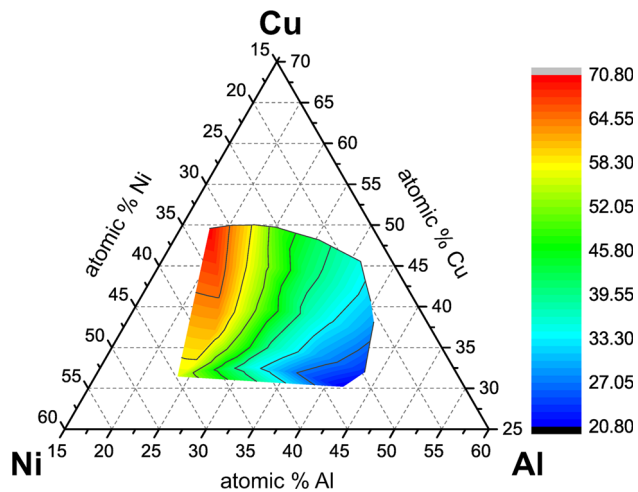


Fig. 5 Total reflectivity of the sample (1064 nm) as a function of chemical composition

and topography analysis was performed and is discussed in Sect. 3.3.

3.3 Thin film morphology and topography

Figure 6 shows micrographs taken at five different areas across the film surface in which different structures are found. The legends shown in Fig. 6a–e are the reflectivity (R), root mean square roughness (σ) and chemical composition (Al, Cu, Ni at.%). The SEM images and the AFM scans are in good agreement in terms of surface characterisation. The results show that, besides the compositional gradient across the surface, the CuAlNi thin film exhibits a morphological gradient as well. In the area with least aluminium (at.%), dominated by a copper–nickel solid solution, the surface is relatively smooth, with surface structures in the range of 10 nm measured in *ImageJ* (Fig. 6a). The results indicate that with an increase in the Al concentration (18–43%), the structures develop and grow in number and size (Fig. 6a–e). In particular, as the structures increase in size (up to ~ 500 nm, shown in Fig. 6d), their surface morphology also changes. They slowly develop “clear-cut” edges. Finally, the Al-rich area is covered in tightly packed, well-defined structures with a smooth texture, which are about 200 nm in size (Fig. 6e). The structures on the sample surface are a consequence of both the compositional gradient [16] and the sputtering process dynamics [17].

The physical dimensions of the structures are considered to understand the correlation between surface morphology and the reduction in reflectivity (as shown in Sect. 3.2). The values for root mean square roughness, σ , and height–height correlation length, T , are given in Table 2. The values indicate a smooth sample surface, with features at least one order of magnitude smaller than the laser

wavelength. The topography with higher σ and T (e.g. sample (8,1) shown in Fig. 6) is hypothesised to increase the absorption by creating a gradual change in the refractive index [18] (i.e. “moth-eye effect”).

3.4 Crater morphology and geometrical analysis after ns laser ablation

The amount of material removed by pulsed laser ablation is related to the energy ratio between the beam input and the damage threshold of the workpiece. To gain insight on the minimum amount of energy needed to ablate the ternary compositional spread, we calculated the ablation threshold of several areas on the sample matrix (as described in [13] for metal films) by using the measured reflectivity and the calculated thermal properties of the sample (based on the concentration and property of each pure metal). The preliminary results indicated that the ablation threshold was strongly dependent on the aluminium atomic percentage in the studied thin film, while the amounts of copper and nickel had a negligible influence. As discussed in Sect. 3.3, the surface morphology is dependent on the Al content through the “moth-eye effect”. Reflectivity is lower where the Al at.% is higher; as the ablation threshold is inversely proportional to the surface reflectivity, this leads to a strong dependence of the ablation threshold on the aluminium percentage. Hence, both the morphological characterisation of the single-pulse ablated craters and the amount of removed material were performed with respect to the Al at.%.

Figure 7 shows the variation of the rim volume (top), crater volume (middle) and resultant ablated volume (bottom) as a function of aluminium concentration. The rim volume (top) is inversely proportional to the amount of Al (*region 1*) up to 27 at.%, where it has a slight increase (*region 2*). The crater and ablated volumes (middle and bottom, respectively) show an inverse correlation with Al content, i.e. both increase rapidly (*region 1*) up to 30% Al, after which they slightly decrease (*region 2*). These two turning points (27 and 30 at.% Al) mark a transition area which is not only observed when quantifying the amount of removed material, but also indicates where the transition in crater morphology takes place.

Figure 7 (bottom) also shows that the lowest amount of removed material (i.e. ablated volume) corresponds to the area with least Al. This can be explained by the similar values of the crater volumes (Fig. 7—middle) and the rim volumes (Fig. 7—top) at lower Al concentration, revealing that material is transported rather than actually removed from the sample. This, together with the quite large error bars (which may be considered evidence of the nonlinear interaction between the beam and the workpiece), indicates that the energy input was close to the ablation threshold of

Fig. 6 SEM images and $3 \times 3 \mu\text{m}^2$ AFM scans of the parent material in several areas across the target surface: **a** (1,8); **b** (5,7); **c** (1,5); **d** (5,5); **e** (8,1). The values for the reflectivity, roughness and chemical composition are given for comparison

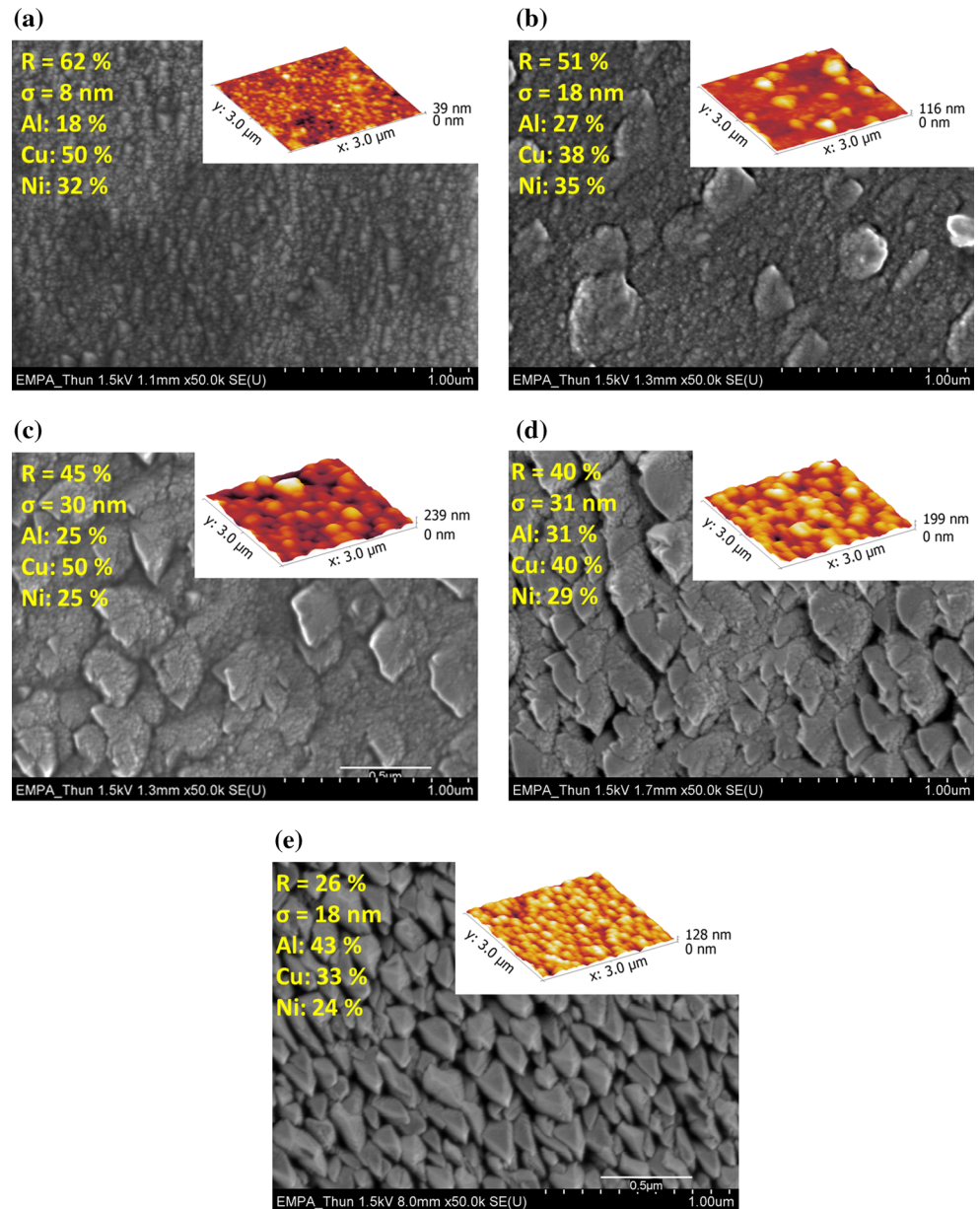


Table 2 Surface parameters of five areas across the sample

Sample ID	σ (nm)	T (nm)
(8,1)	18	80
(5,5)	31	138
(1,5)	30	179
(5,7)	18	214
(1,9)	8	286

the sample. With further addition of aluminium, the ablated volume increases up to the maximum value of $\sim 1500 \mu\text{m}^3$, suggesting that the sample absorbed more energy than the ablation threshold value. The subsequent decrease in the resultant ablated volume is caused by both diminishing of the crater volume itself and the built-up of

melt around the craters. To illustrate the behaviour of both variations of crater melt and crater geometry, crater profiles corresponding to *region 1*, *region 2* and the transitional area are shown in Fig. 8.

The reduced amount of removed material after the maximum value found at $\sim 30\%$ Al (at.%) could be explained by an increase in the optical density of plasma, which absorbs the laser radiation. In other words, when irradiating a metal with ns IR laser pulses in atmospheric conditions, plasma formation threshold was reported to be just $0.1\text{--}0.2 \text{ J/cm}^2$ higher than the ablation threshold [15, 19]. Thus, with the lower ablation threshold, as the laser reached the workpiece more material was vaporised, leading to the formation of a dense cloud in front of the target. The plasma is ignited and, depending on its density,

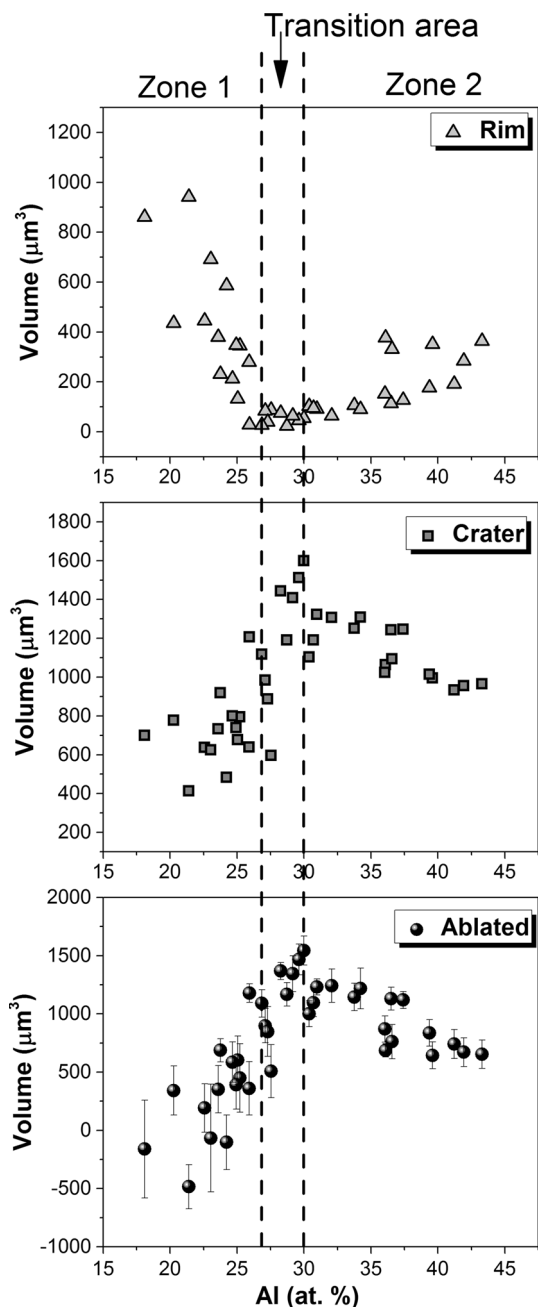


Fig. 7 Rim (volume above the surface)—*top*, crater (volume below surface)—*middle* and resultant ablated volume—*bottom*, as a function of aluminium atomic percentage

absorbed a certain amount of the incoming laser radiation [20]. The smaller the ablation threshold, the more material vaporises early in the process, and the more absorbent the plume becomes.

Along with the ablated volume, crater shape and morphology gradually change across the sample surface, with transitional features observed in areas with 27–30% aluminium at.%. By using the similarities observed in shape, re-deposited material and the quantities of material

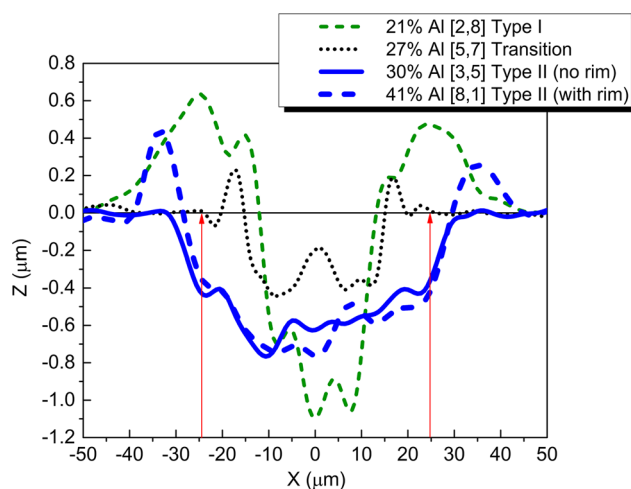


Fig. 8 Evolution of typical crater profiles with an increase in Al percentage. $Z = 0$ represents the surface of the thin film, and the *red arrows* indicate the beam diameter at the target surface

removed, two categories of craters have been identified, corresponding to *region 1* and *region 2* discussed in Fig. 7. Craters in *region 1* (“Type I” in Fig. 8) are narrower and deeper than craters in *region 2* (“Type II” in Fig. 8) and have a significant amount of re-solidified material on the edge. The shape changes in the transitional area (“Transition” in Fig. 8) between *region 1* and *region 2*, as the craters become wider and shallower, and the rim of re-solidified material significantly decreases. Craters in *region 1* exhibit a relatively smooth crater bottom, up to the transition area (as shown in Fig. 9a—right-hand side), after which all the craters (found in *region 2*) exhibit an interconnected porous surface, which appears to be re-solidified material “frozen in motion” (Fig. 9b—right-hand side). In addition to the composition of the thin film, we attributed the change in crater shape for craters in *region 2* to the columnar structure of the parent material (Fig. 9b—left-hand side). This morphology may decrease the thermal contact between the thin film and the substrate (i.e. higher thermal contact resistance), reducing heat losses to the substrate compared to craters in *region 1*.

4 Conclusions

Our aim is to report one of the first studies on the interaction between a beam of constant parameters (Nd:YAG, 1064 nm, 30-ns pulse duration, 50 μm beam diameter and 4.54 J/cm^2 fluence) and a ternary alloy compositional spread (Cu: 30–50 at.%, Al: 18–43 at.%, Ni: 18–45 at.%, thickness ~ 1 –1.35 μm). This novel approach could expand the understanding of the interaction between laser and combinatorial materials and, at the same time, be of

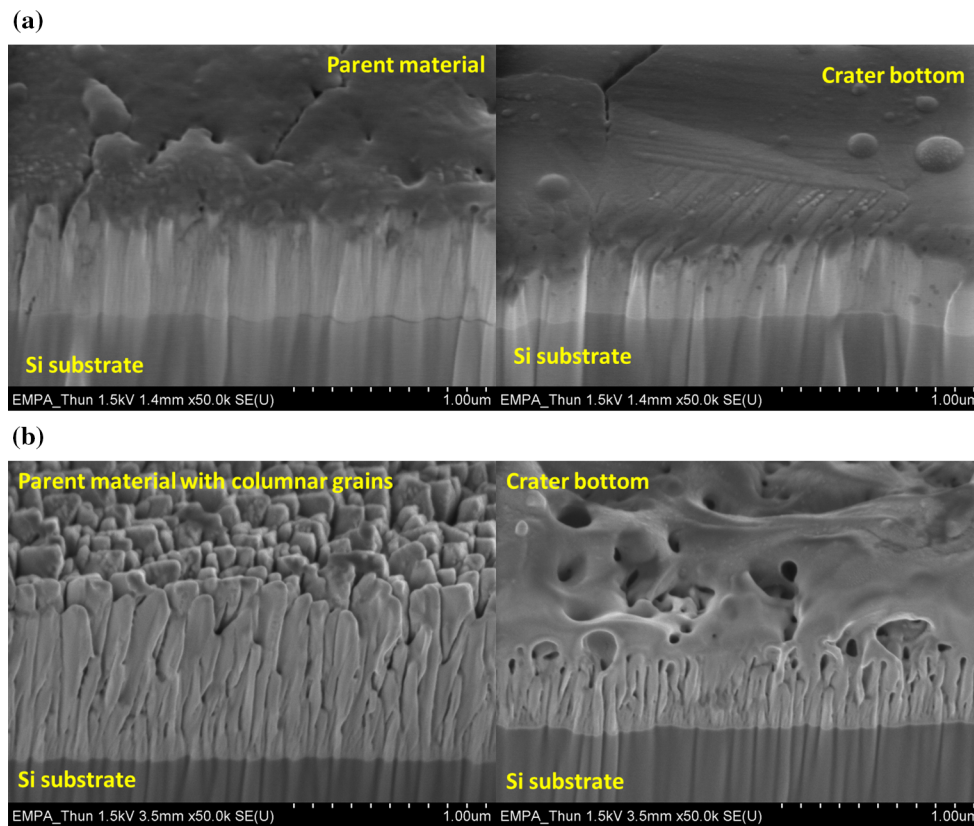


Fig. 9 SEM images of cross sections of the parent material (*left*) and crater (*right*) in **a** region 1/transition area and **b** region 2, showing the typical morphology

use to both material scientists and engineers in developing new applications.

Preliminary calculations showed that the ablation threshold decreases with an increase in the aluminium percentage. Besides the compositional gradient, the target had a morphological gradient as well, which was similar to the distribution of aluminium in the sample. The structures varied in size (from 10 to 500 nm) and shape, and their presence might have played a role in both the decrease in the sample reflectivity (at 1064 nm) and the thermal contact between the thin film and the silicon substrate.

Based on the variations found in the geometrical and morphological characteristics of the craters and the sub-surface changes, as well as on the variations in the ablated volume, two regions were identified, separated by a transition area (between 27 and 30 at.% Al).

In the first region, the ablated volume was proportional to the amount of aluminium in the sample; the craters were deeper and narrower and the sub-surface was noticeably affected by heat; a higher amount of re-deposited material compared to the second region was present, which indicated that the energy delivered by the beam was close to the ablation threshold.

In the second region, the craters were wider and shallower, and the sub-surface showed little heat damage; the variation of the volume was inversely proportional to the amount of aluminium, despite the threshold continuously decreasing. We have attributed this behaviour to the increase in plasma density followed by partially decoupling of the workpiece from the incoming laser radiation.

Acknowledgements We would like to acknowledge the funding support of EUFP7-ITN (Grant No. 316560) for the works presented as a part of the STEEP project. We acknowledge the initial laser ablation test was carried out at the University of Liverpool and Bogdan Rusu (“Al. I. Cuza” University of Iași) for help with the AFM measurements. We would like to thank our colleagues Stefano Buratin (University of Birmingham) and Gaurav Mohanty (EMPA) for the useful discussions and support, as well as our project coordinator Dragoș Axinte (University of Nottingham) for reviewing the first manuscript.

Open Access This article is distributed under the terms of the Creative Commons Attribution 4.0 International License (<http://creativecommons.org/licenses/by/4.0/>), which permits unrestricted use, distribution, and reproduction in any medium, provided you give appropriate credit to the original author(s) and the source, provide a link to the Creative Commons license, and indicate if changes were made.

References

1. J. Meijer, J. Mater. Process. Technol. **149**, 2 (2004)
2. M.D. Shirk, P.A. Molian, J. Laser Appl. **10**, 18 (1998)
3. C.P. Grigoropoulos, *Transport in Laser Microfabrication: Fundamentals and Applications* (Cambridge University Press, New York, 2009), p. 400
4. P. Schaaf (ed.), *Laser Processing of Materials: Fundamentals, Applications and Developments* (Springer, New York, 2010)
5. K. Sokolowski-Tinten, J. Bialkowski, A. Cavalleri, D. von der Linde, A. Oparin, J. Meyer-ter-Vehn, S. Anisimov, Phys. Rev. Lett. **81**, 224 (1998)
6. A.V. Pakhomov, M.S. Thompson, D.A. Gregory, J. Phys. D Appl. Phys. **36**, 2067 (2003)
7. S. Fähler, H.-U. Krebs, Appl. Surf. Sci. **96–98**, 61 (1996)
8. X. Xu, K.H. Song, Mater. Sci. Eng. A **292**, 162 (2000)
9. G. Heise, M. Englmaier, C. Hellwig, T. Kuznicki, S. Sarrach, H.P. Huber, Appl. Phys. A Mater. Sci. Process. **102**, 173 (2011)
10. S.N. Aqida, D. Brabazon, S. Naher, Z. Kovacs, D.J. Browne, Appl. Phys. A Mater. Sci. Process. **101**, 357 (2010)
11. O.A. Bulgakova, N.M. Bulgakova, V.P. Zhukov, Appl. Phys. A Mater. Sci. Process. **101**, 53 (2010)
12. S. Rung, A. Christiansen, R. Hellmann, Appl. Surf. Sci. **305**, 347 (2014)
13. E. Matthias, M. Reichling, J. Siegel, O.W. Kading, S. Petzoldt, H. Skurk, P. Bizenberger, E. Neske, Appl. Phys. A Mater. Sci. Process. **58**, 129 (1994)
14. C.P. Kothandaraman, S. Subramanyan, *Heat and Mass Transfer Data Book*, 5th edn. (New Age International, New Delhi, 2004)
15. O. Benavides, O. Lebedeva, V. Golikov, Opt. Express **19**, 21842 (2011)
16. M. Hafner, W. Burgstaller, A.I. Mardare, A.W. Hassel, Thin Solid Film. **580**, 36 (2015)
17. J. A. Thornton, in *Proceedings of the SPIE 0821, Model. Optical Thin Film*. **95** (1988)
18. B. Hua, Q.F. Lin, Q.P. Zhang, Z.Y. Fan, Nanoscale **5**, 6627 (2013)
19. O. Benavides, L.C. de La May, A.F. Gil, Opt. Soc. Am. **21**, 13068 (2013)
20. J.M. Vadiello, J.M. Fernández Romero, C. Rodríguez, J.J. Laserna, Surf. Interface Anal. **27**, 1009 (1999)
21. A.J. Bradley, H. Lipson, Proc. R. Soc. London **167**, 421 (1938)